APL Energy

RESEARCH ARTICLE | MAY 22 2026

Solution-processed bandgap tunable kesterite absorbers for low-cost and eco-friendly thin film solar cells

Special Collection: Energy Materials for Extreme Environments

Mina Ghorbani ; Sunil Suresh; Gautam Virenutan; Guy Brammertz ; Vishal Kakkarakunnel Jose; Daniely Santos ; Irene Dei Tos; Bárbara Sieira ; Jennifer Teixeira ; Pedro Salomé; Sudhanshu Shukla ; Bart Vermang

APL Energy 4, 026101 (2026)
https://doi.org/10.1063/5.0325153

Solution-processed bandgap tunable kesterite absorbers for low-cost and eco-friendly thin film solar cells

Cite as: APL Energy 4, 026101 (2026); doi: 10.1063/5.0325153
Submitted: 29 January 2026 • Accepted: 5 May 2026 •
Published Online: 22 May 2026

Mina Ghorbani,[1,2,3,a] Sunil Suresh,[1,2,3] Gautam Virenutan,[1,2,3] Guy Brammertz,[1,2,3] Vishal Kakkarakunnel Jose,[1,2,3] Daniely Santos,[1,2,3] Irene Dei Tos,[1,2,3] Bárbara Sieira,[4] Jennifer Teixeira,[4] Pedro Salomé,[4] Sudhanshu Shukla,[1,2,3,a] and Bart Vermang[1,2,3]

AFFILIATIONS

[1] imec, IUMAT, Thor Park 8320, B-3600 Genk, Belgium
[2] Hasselt, Institute for Materials Research (IUMAT), Martelarenlaan 42, B-3500 Hasselt, Belgium
[3] EnergyVille, IUMAT, Thor Park 8320, B-3600 Genk, Belgium
[4] INL—International Iberian Nanotechnology Laboratory, Avenida Mestre José Veiga, 4715-330 Braga, Portugal

Note: This paper is part of the Special Topic on Energy Materials for Extreme Environments.
[a] **Authors to whom correspondence should be addressed:** sudhanshu.shukla@imec.be and Mina.ghorbani@imec.be

ABSTRACT

Cu_2ZnSnS_4 (CZTS) is a promising kesterite semiconductor for sustainable photovoltaic applications, offering advantages such as high optical absorption, bandgap tunability, and eco-friendly, earth-abundant elements. However, while solution-processed CZTS has shown potential, key gaps remain in understanding their optoelectronic properties, particularly how sulfur (S) and selenium (Se) influence phase segregation and bandgap grading. Furthermore, the wide-bandgap CZTS suffers from a significant open-circuit voltage (V_{OC}) deficit, limiting its efficiency. In this study, we fabricated solution-processed wide-bandgap $Ag_{0.1}(Cu_{0.9})_2$ $ZnSnS_4$ solar cells, achieving a remarkably high V_{OC} of 770 mV [58.5% of (V_{OC}^{SQ})]. We compared the pure-sulfide wide-bandgap films, which formed a single kesterite layer, with narrow-bandgap $Ag_{0.1}(Cu_{0.9})_2ZnSn(S,Se)_4$ films, which exhibited a dual-layer structure. Advanced characterization techniques, including scanning electron microscopy and scanning transmission electron microscopy, revealed Zn-rich and Sn-rich phase segregation for narrow-bandgap films, while back-side Raman spectroscopy showed depth-dependent compositional gradients. The incorporation of Se in the narrow-bandgap films led to improved carrier dynamics, reduced defect density, and enhanced device performance, with a significant increase in efficiency compared to the wide-bandgap films. These findings emphasize how S and Se tuning can modulate phase behavior, enabling the design of CZTSSe materials with tailored bandgaps and optimized optoelectronic properties for high-efficiency, environmentally sustainable solar cells.

INTRODUCTION

Progressive energy demand and limited stock of conventional energy sources have created an urgency to develop techniques that can harness alternative energy sources. Among the available renewable energy sources, solar energy stands out as a prominent and reliable option for large-scale energy generation. To address the energy demand with solar energy, solar cells are employed to convert sunlight into electricity, the most utilizable form of energy.[1] Photovoltaic (PV) technologies have traditionally been dominated by crystalline silicon; however, the field is rapidly evolving toward application-specific systems that extend beyond rigid, utility-scale modules.[2,3] In particular, emerging applications, such as building-integrated photovoltaics (BIPV), portable electronics, and indoor energy harvesting, are driving the development of lightweight, flexible, and low-cost solar cell technologies.[4]

Thin-film photovoltaic technologies are well positioned to address these emerging demands due to their low material consumption, compatibility with large-area deposition, and potential for integration onto flexible and unconventional substrates.[2,4] Within

this context, kesterite has emerged as a promising absorber material owing to its composition of earth-abundant, non-toxic elements and its favorable optoelectronic properties, including a high absorption coefficient and a tunable direct bandgap.[5–7] Beyond these intrinsic advantages, kesterite materials are particularly attractive for next-generation PV applications because they are compatible with solution-based and low-temperature fabrication routes, enabling scalable deposition on lightweight and flexible substrates.[7,8]

Recent advances have further highlighted the potential of kesterite absorbers for flexible and integrated photovoltaic systems. Solution-processable precursor chemistries enable scalable deposition techniques such as spin coating, printing, and spray coating, which are compatible with roll-to-roll manufacturing and large-area production.[4,7] These attributes make kesterite a strong candidate for urban-integrated energy systems, where conformability, weight reduction, and cost-effective manufacturing are critical.[4] Concurrently, significant progress in device engineering has led to a rapid improvement in power conversion efficiencies, with recent reports exceeding the 15% threshold, marking an important milestone in the development of kesterite photovoltaics.[9] Tandem solar cells require a stack of narrow and wide bandgap solar cells. Narrow-bandgap kesterite absorbers have undergone extensive optimization, resulting in a substantial improvement in power conversion efficiency from 13.86% to 15.45%[10] and certified 15.1% device efficiency.[11] In contrast, wide-bandgap kesterite solar cells remain comparatively underexplored, with performance historically plateauing at ~11%.[12] Only recently has progress been reported, with certified total-area efficiencies reaching ~13.2%.[13]

Despite these advances, the performance of kesterite solar cells remains fundamentally limited by a large open-circuit voltage (V_{OC}) deficit, particularly in wide-bandgap compositions required for tandem and indoor photovoltaic applications.[8] In CZTS compounds, antisite defects, such as Cu atoms occupying Sn sites (Cu_{Sn}^{3-}) and Sn atoms occupying Zn sites (Sn_{Zn}^{2+}), tend to form deep electronic states within the bandgap.[14] These defects also have relatively low formation energies in stoichiometric CZTS, particularly when they associate with other energetically favorable compensating defects and they are believed to contribute significantly to carrier recombination losses and limiting achievable device efficiencies.[14]

To mitigate these limitations, compositional engineering strategies, such as cation substitution, and alloying have been widely explored to suppress defect formation and optimize the electronic structure of the absorber layer.[11,15] These concepts could be easily explored via solution processing techniques with suitable elements from the Periodic Table, such as Li, Ag, Cd, Ge, and many more. In this regard, solution processing offers a unique advantage over vacuum-based fabrication methods by enabling molecular-level mixing of precursor species, allowing precise control over composition, defect chemistry, and film formation kinetics. Furthermore, solution-based approaches provide flexibility in tuning crystallization behavior, grain growth, and interface properties, which are critical for improving device performance.[8] Importantly, these methods are inherently compatible with scalable manufacturing processes and offer a pathway toward low-cost, large-area, and flexible photovoltaic technologies suitable for next-generation energy applications.[16]

Building on the advantages of solution-processable kesterite absorbers for scalable and application-specific photovoltaics, this work systematically investigates both narrow- and wide-bandgap kesterite solar cells fabricated via a unified solution-based approach. A molecular ink strategy, based on metal salts, thiourea, and 2-methoxyethanol, is employed to enable homogeneous precursor formation and precise compositional control. In this context, the primary objective of this work is to perform a comparative evaluation of the structural and optoelectronic properties of ink-derived kesterite absorbers with narrow and wide bandgaps. By employing a unified ink-based deposition strategy, this study aims to establish a direct correlation between processing pathways and optoelectronic properties, thereby providing insights relevant to bandgap engineering and the development of kesterite materials for tandem and application-specific photovoltaic technologies. For narrow-bandgap absorbers, Ag-alloyed $Cu_2ZnSn(S,Se)_4$ (ACZTSSe) thin-films are realized through selenization of spin-coated precursor layers, following established high-efficiency processing routes.[17] In contrast, wide-bandgap Ag–Cu_2ZnSnS_4 (ACZTS) absorbers are obtained via sulfurization under H_2S atmosphere, allowing direct comparison of chalcogen-dependent crystallization pathways within the same processing framework. Importantly, the use of H_2S gas as a sulfur source enables enhanced control over film formation, yielding improved compositional uniformity and reduced defect density compared to conventional sulfur powder-based approaches.[18–20] This controlled sulfurization environment also provides a unique opportunity to modulate reaction kinetics, as the slower crystallization dynamics facilitate partial decoupling of nucleation and grain growth processes. Such control is particularly relevant for defect engineering in wide-bandgap kesterite, where recombination losses remain a critical limitation. The insights gained from this comparative study not only advance the understanding of chalcogen-dependent crystallization mechanisms in solution-processed kesterite systems but also establish a versatile pathway for tailoring absorber properties toward high-efficiency, lightweight, and potentially flexible photovoltaic applications.

EXPERIMENTAL DETAILS

Chemicals

Copper(I) chloride (CuCl, ≥99.995%, Sigma-Aldrich), silver(I) chloride (AgCl, 99.999%, Sigma-Aldrich), zinc(II) acetate [$Zn(Ac)_2$, 99.99%, Sigma-Aldrich], tin(IV) chloride ($SnCl_4$, 99.995%, Sigma-Aldrich), thiourea (TU, 99.1%, analytical reagent), 2-methoxyethanol (2-ME, 99.8%, anhydrous, Sigma-Aldrich), selenium-pellets, and H_2S-gas (≥99.5, Praxair NV) were used as received without further purification.

Device fabrication

A molecular ink was prepared following the method reported by Zhou *et al.*[17] In brief, 717.76 mg of CuCl and 115.45 mg of AgCl were dissolved in 5 ml of 2-ME containing 2100 mg of TU (ink-1). In a separate vial (ink-2), 1040.6 mg of $Zn(Ac)_2$ and $SnCl_4$ were dissolved in 5 ml of 2-ME. Both solutions were stirred at room temperature until complete dissolution of the precursors. Subsequently, the two solutions were combined to obtain a final precursor ink (10 ml total volume). The final ink composition was adjusted to achieve the following stoichiometry: [Ag]/[Ag] + [Cu] = 0.1, ([Ag]

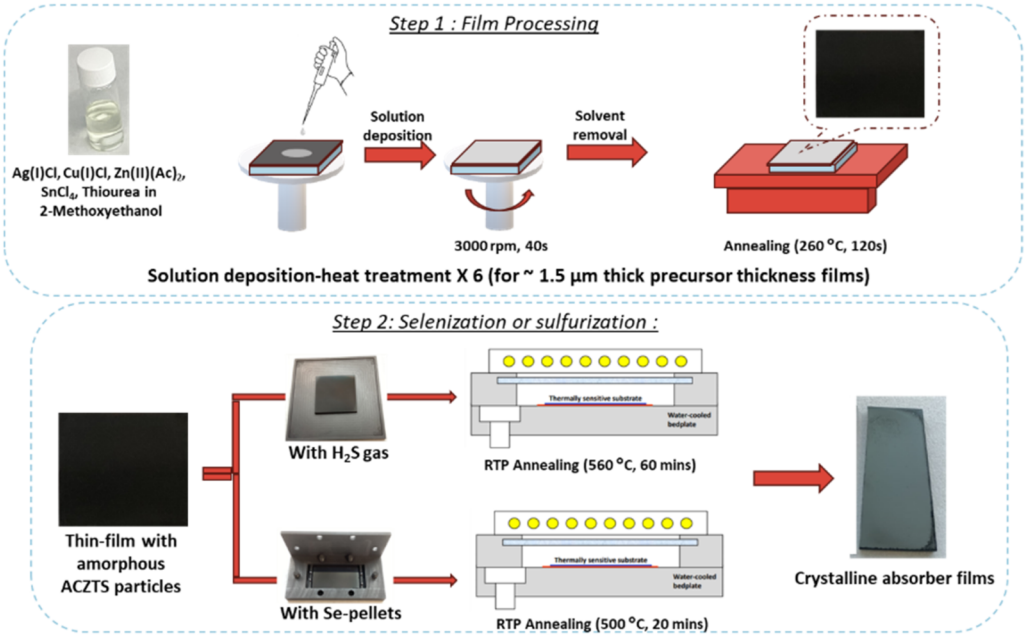

FIG. 1. Schematic illustration of ACZTS and ACZTSSe thin-film fabrication.

+ [Cu])/([Zn] + [Sn]) = 0.75, [Zn]/[Sn] = 1.12, and [TU]/[metals] = 2.25.

The Mo-coated soda-lime glass (SLG/Mo) substrates were sequentially cleaned by ultrasonication (10 min each) in detergent solution, deionized water, acetone, and isopropanol. The precursor ink was then spin-coated onto the substrates at 3000 rpm for 40 s. After each coating cycle, the films were dried on a hot plate at 260 °C for 2 min. This process was repeated six times to achieve the desired thickness.

All thermal treatments were carried out using a rapid thermal processing (RTP) system in Annealsys AS-One system. For the fabrication of narrow-bandgap absorbers, the precursor films were selenized in a graphite box containing 100 mg of Se pellets. The samples were heated to 500 °C at a ramp rate of 0.7 °C s^{-1} and held for 20 min. For wide-bandgap absorbers, sulfurization was performed under an H_2S-containing atmosphere. A diluted H_2S/N_2 gas mixture (H_2S:N_2 = 1:20) was used as the sulfur source at a total pressure of 800 mbar. For safety reasons, the H_2S flow was carefully regulated using mass flow controllers and operated under continuous ventilation with appropriate gas scrubbing to ensure safe exhaust handling. The temperature was ramped at a rate of 0.7 °C s^{-1} up to 550 °C, held for 1 h to ensure complete crystallization and sulfur incorporation into the kesterite lattice. After annealing, the system was allowed to cool naturally to room temperature under the same controlled atmosphere to avoid thermal shock and preserve film integrity. The samples of Ag-doped $Cu_2ZnSn(S,Se)_4$ and Ag-doped Cu_2ZnSnS_4 thin-films are hereafter referred to as ACZTSSe and ACZTS, respectively. A schematic illustration of the thin-film fabrication process is shown in Fig. 1. To fabricate the solar cells, 50 nm of the cadmium sulfide (CdS) layer was deposited on the kesterite films via the chemical bath deposition (CBD) method. Subsequently, 60 nm of the intrinsic zinc oxide (i-ZnO) layer and 150 nm of the indium tin oxide (ITO) layer were deposited via sputtering using the recipe mentioned elsewhere.[21] The full stack architecture for device is Mo/absorber/CdS/i-ZnO/ITO. No additional metallic grid was used; thus, the series resistance is partially influenced by the sheet resistance of the ITO layer.

Characterization methods

X-ray diffraction (XRD) was carried out using a Bruker D8 diffractometer using Cu Kα radiation (λ = 0.154 06 nm) to identify the crystal structure of the ACZTS and ACZTSSe. Furthermore, Raman spectroscopy was conducted using a 532 nm laser on a HORIBA Jobin spectrometer equipped with a Symphony detector to investigate structural changes. For optical properties measurement, steady-state photoluminescence (PL) was measured using a PicoQuant FluoTime 300 setup, covering the range of 600–1400 nm. Time-resolved photoluminescence (TRPL) was measured at 980 and 1160 nm for ACZTS and ACZTSSe films, respectively, with an excitation wavelength of 532 nm (25 ps, 3 MHz). The surface morphology and cross-sectional structure of the kesterite thin films were examined using scanning electron microscopy (SEM, VEGA3 TESCAN). The elemental compositional study was performed using an energy-dispersive x-ray (EDX, Bruker) detector integrated with the SEM tool. The High-Angle Annular Dark-Field Scanning Transmission Electron Microscopy (HAADF STEM) analysis of the device was conducted using a FEI Titan G3 Cubed Themis, operating at 200 kV. Energy dispersive x-ray spectroscopy (EDS) analysis was performed through a double-corrected FEI Titan G3 Cubed Themis equipped with a Super-X EDX System, at 200 kV. EDS line profiles for the Cu, Zn, Sn, S, Se, and Mo were plotted, using the

following spectrum lines: Cu Kα = 8.04 keV, Zn Lα = 1.01 keV, Sn Lα = 3.44 keV, S Kα = 2.31 keV, Se Kα = 11.22 keV, and Mo Lα = 2.29 keV. The performance of the solar cells was analyzed by measuring current density–voltage (J–V) curves using a 4-point probe setup (Keithley 2401 SourceMeter) and an Oriel solar simulator to replicate the AM1.5G illumination spectrum. External quantum efficiency (EQE) measurements were performed on a Bentham PVE300 PV tool, covering the range of 350–1300 nm with a 10 nm step.

RESULTS AND DISCUSSION

The surface morphology of ACZTS and ACZTSSe thin-films was investigated using top-view SEM imaging, as shown in Figs. 2(a) and 2(b), respectively. The SEM images reveal significant differences in surface morphology and grain size between the two samples. Statistical analysis using ImageJ yields an average grain size of 1.085 μm for ACZTS and 1.859 μm for ACZTSSe. The larger grain size in ACZTSSe can be attributed to enhanced crystallization kinetics during selenization, which promotes grain growth compared to sulfurization. Both films exhibit dense and compact morphologies with uniform surface coverage. However, the ACZTSSe film consists of larger, irregularly shaped grains, whereas the ACZTS film shows comparatively smaller and more uniformly distributed grains with a near-equiaxed morphology. The cross-sectional SEM images of ACZTS and ACZTSSe samples, shown in Figs. 2(c) and 2(d), reveal distinct differences in morphology and grain size. The ACZTS sample [Fig. 2(c)] exhibits a single-layer structure, where some grains span the entire thickness of the layer, extending from the top to the bottom. This layer, deposited on Mo-coated glass, has a thickness of ~1.0 μm. In contrast, the ACZTSSe sample displays a double-layer structure, consisting of a top layer with large grains and a bottom layer with smaller grains, as illustrated in Fig. 2(d). The combined thickness of these layers is ~1.2 μm, with each layer contributing roughly half of the total thickness. The top layer is Se-rich, while the bottom layer remains S-rich, likely due to the insufficient penetration of Se vapor during the selenization process. This limited diffusion prevents complete S replacement in the lower region, resulting

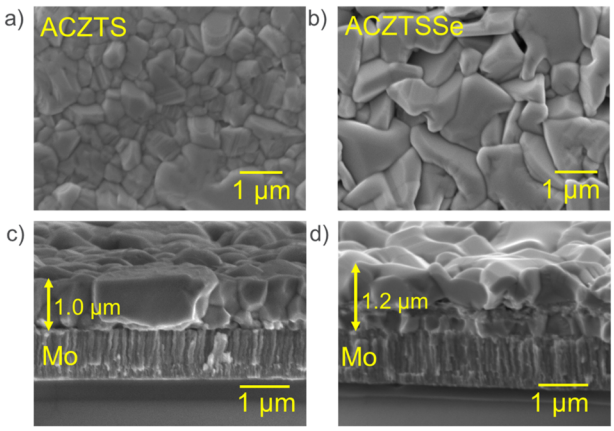

FIG. 2. SEM images showing the top view of (a) ACZTS and (b) ACZTSSe films, and the cross-sectional view of (c) ACZTS and (d) ACZTSSe films.

TABLE I. EDS estimated composition analysis of ACZTS and ACZTSSe thin-films.

Films	[Ag]/([Ag] + [Cu])	([Ag] + [Cu])/([Zn]+[Sn])	[Zn]/[Sn]	[S]/([S] + [Se])
Precursor	0.09	0.72	1.24	1.0
ACZTS	0.08	0.94	1.13	1.0
ACZTSSe	0.11	0.76	1.17	0.17

in the observed layered morphology. The cross-sectional morphology of the ACZTSSe sample suggests that a high Se vapor partial pressure promotes the formation of large, compact grains in the top layer during selenization. However, this compact structure impedes the diffusion of Se to the bottom layer and the upward diffusion of Zn to the surface. Consequently, poor crystallization and Se deficiency occur in the lower region of the ACZTSSe film, contributing to the formation of the distinct double-layer structure.[22]

The estimated chemical compositions of two thin-film samples, ACZTSSe and ACZTS, as determined by EDX analysis, are presented in Table I. Both samples exhibit Cu-poor [Cu/(Zn + Sn) < 1] and Zn-rich (Zn/Sn > 1) compositions. The composition of the precursor films closely matched the prepared ink composition, as detailed in the experimental section. The Cu_2ZnSnS_4 precursor films successfully meet the Zn-rich composition requirement following sulfurization. Similarly, the metal stoichiometry of the ACZTSSe films was well preserved, aligning closely with that of the precursor films. In contrast, the ACZTS films exhibited slight deviations in stoichiometry due to the loss of Zn and Sn elements, which form volatile secondary phases during the sulfurization process.[23,24] Beyond metal stoichiometry, EDX analysis provided valuable insights into the chalcogen ratio, specifically [S]/([S] + [Se]), which indicated the extent of S replacement by Se. This substitution not only alters the composition but also results in a narrower bandgap, enabling enhanced absorption of a broader spectrum of sunlight and thereby improving overall device performance.[25] The higher formation energy of Cu_{Zn} defects in ACZTS compared to V_{Cu} makes Cu-poor/Zn-rich compositions advantageous for improving carrier transport efficiency. Excessive Cu content can lead to the formation of Cu_2S secondary phases, which, while highly conductive, significantly increase the risk of short-circuiting. Under Cu-poor conditions, V_{Cu} becomes the dominant defect, effectively suppressing the creation of deep-level defect pairs, such as (Cu_{Zn} + Sn_{Zn}) and (2Cu_{Zn} + Sn_{Zn}). This suppression enhances carrier transport and improves the device's photoelectric conversion efficiency (PCE). In addition, under Zn-rich conditions, the formation of secondary phases, such as Cu_2SnS_3, which has a low optical bandgap and promotes carrier recombination, is minimized. This reduction in recombination further contributes to efficient carrier dynamics. Therefore, adopting Zn-rich conditions during the preparation of ACZTS thin-films is essential for achieving higher PCE in devices.

XRD was used to investigate the crystalline properties of the thin films, and the results are illustrated in Fig. 3(a). The XRD pattern of the ACZTS film, indexed according to JCPDS No. 26-0575, confirms the formation of the kesterite phase, with prominent diffraction peaks located at 28.32°, 47.00°, and 55.74°, corresponding to the (112), (220), and (312) crystallographic, respectively.[26]

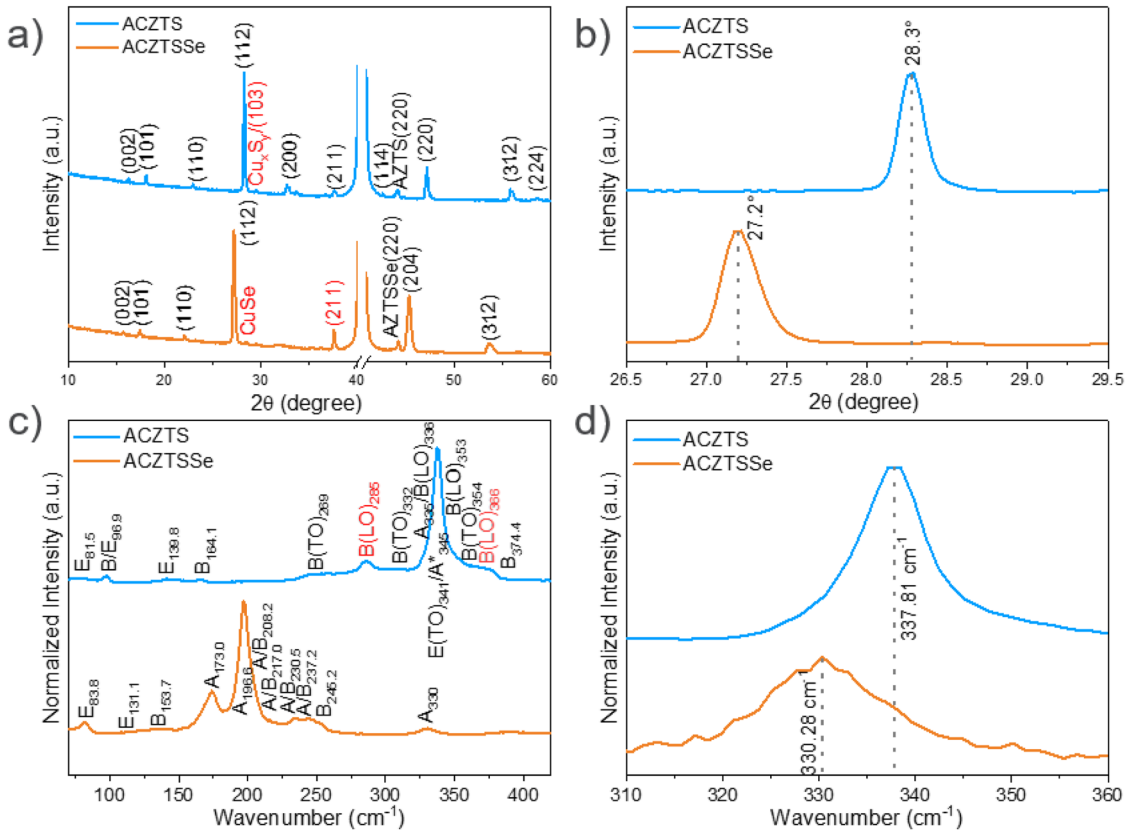

FIG. 3. (a) XRD patterns, (b) magnified view of the (112) diffraction peaks, (c) normalized Raman spectra, and (d) enlarged Raman peaks of ACZTS and ACZTSSe films.

A weak additional peak at 44.10° is attributed to the presence of minor Ag_2ZnSnS_4 secondary phase.[27] The intense peak at 40° corresponds to the (110) reflection of the Mo substrate. Figure 3(a) displays the XRD pattern of the ACZTSSe sample, the (112) diffraction peak shifts to a lower angle compared to the ACZTS thin-film, which is indicative of the incorporation of Se^{2-} ions into the kesterite lattice. The larger ionic radius of Se^{2-} compared to S^{2-} causes an expansion of the lattice constant, leading to the observed peak shift. Notably, the shift of the (112) peak from 28.32° to 27.20° [as illustrated in Fig. 3(b)], the (220) peak from 47.00° to 45.26°, and the (312) peak from 55.74° to 53.51° in the ACZTSSe film further confirms the successful incorporation of Se into the kesterite lattice, which aligns with the EDX results. In addition, after the incorporation of Se, the impurity phase $Cu_{2-x}S$ was replaced by $Cu_{2-x}Se$. This may suggest that, in the presence of both S and Se in the reaction medium, they compete to react with metal ions, particularly Cu, forming Cu-based binary compounds. The preferential formation of Cu-based secondary phases can be attributed to the higher reactivity and relatively high mobility of Cu ions compared to Sn and Zn ions.[28] We note that the minor Cu–S/Se peaks in our XRD likely arise from localized Cu excess and limited reaction kinetics. Recent studies show that low S/Se ratios or insufficient annealing strongly favor the formation of binary Cu chalcogenides. For example, Xu *et al.* found that under low Se vapor, Cu_2Se (and associated Cu_xSe phases) form instead of kesterite.[29] Similarly, the elemental mapping of high-efficiency CZTSe cells revealed Cu-rich grains ($Cu_{2-x}Se$) at the Mo interface.[30] These conductive Cu–chalcogen phases introduce shunt paths and deep trap states, reducing V_{OC} and fill factor (FF). Importantly, Li *et al.* demonstrated that blocking Cu diffusion to Mo (via a 1-nm Al_2O_3 layer) suppressed $Cu_{2-x}Se$ formation and improved V_{OC} by ~90 mV.[31] We, therefore, attribute our observed $Cu_{2-x}S(e)$ to residual Cu-rich regions and limited reaction kinetics. The following strategies can mitigate the formation of such phases: controlling stoichiometry to be Cu-poor [Cu/(Zn + Sn) ≈ 0.85–0.90] to prevent $Cu_{2-x}S$ crystallization,[32] increasing the sulfurization temperature and time to drive complete reaction (prevents Cu_2S phase formation when sulfurizing at >550 °C[29]), and applying a short KCN etch as a surface treatment.

To further validate the phase formation, Raman spectroscopy was conducted. Figure 3(c) shows the Raman spectrum of the ACZTS sample. It revealed an intense peak at 337 cm^{-1}, accompanied by two shoulders at 285 and 375 cm^{-1}, which correspond to the main vibrational modes of the CZTS phase.[33] The strongest peak at 337 cm^{-1} is attributed to the A symmetry mode, while 285 and 375 cm^{-1} peaks are assigned to the B and/or E symmetry modes. The Raman spectrum of the ACZTSSe sample displayed three main peaks at 173, 196, and 233 cm^{-1}, which is shown in Fig. 3(c). The peak at 196 cm^{-1} is assigned to the A_1 symmetry mode, while the

weaker peak at 232 cm^{-1} corresponds to the B and/or E symmetry modes. An additional peak at 330 cm^{-1} was observed in the ACZTSSe sample, which is related to vibrations of the S atoms in the lattice. Due to the coexistence of S and Se in the tetragonal unit cell, the main peak of pure CZTSe, typically observed at 192 cm^{-1}, shifted to a higher frequency at 196 cm^{-1}, while the characteristic peak of ACZTS at 336 cm^{-1} shifted to a lower wavenumber of 330 cm^{-1}, as shown in Fig. 3(d). These shifts are consistent with the XRD results and aligns with the findings of Dimitrievska *et al.*, who attributed the shift to the substitution of ~80% of S with Se[26,34] Together, these results indicate the successful incorporation of both S and Se into the kesterite structure.

Figure 4 shows representative HAADF STEM and STEM-EDS mapping images of both absorber layers deposited on Mo-coated glass. The ACZTSSe thin-film exhibits a double layer structure compatible with the SEM images, with a low [S]/([S] + [Se]) in the upper region and a S-rich region on the bottom, in contrast with the homogeneous distribution of S observed for the ACZTS sample. Moreover, from the STEM-EDS mapping analysis, it can be seen that Se is widely distributed throughout the ACZTSSe layer, even though there were challenges in introducing S. It is important to mention that the S Kα line value is near the Mo Lα line, as illustrated in Fig. 4, and this should be considered to prevent any misleading conclusions.

Even though the element distribution seems balanced, a closer look at the Cu, Zn, and Sn maps shows that there are Cu-rich areas, having noticeably lower levels of Zn and Sn in the ACZTSSe absorber, while for ACZTS one, in contrast, Sn is widely found throughout the Cu-rich zone. This suggests that the addition of Se alters the distribution of Zn, shifting it from the Cu-rich area in the ACZTS sample to the Cu-poor area in ACZTSSe. In addition, when examining the distribution of Cu and Se or S, it becomes evident that the elemental distribution may promote the formation of $Cu_{2-x}S$ and $Cu_{2-x}Se$, for ACZTS and ACZTSSe, respectively, which aligns with the XRD results mentioned earlier.

The PL and TRPL analyses were performed at room temperature to evaluate the optical properties of the ACZTS and ACZTSSe thin-films. The PL results, presented in Fig. 5(a), reveal that the ACZTSSe films exhibit significantly higher PL intensity than the ACZTS films. This disparity is attributed to a higher defect density in the ACZTS films, as defects promote non-radiative recombination, thereby suppressing PL intensity. In semiconductor films, PL intensity is governed by the balance between radiative and non-radiative relaxation pathways of excited carriers.[35] A higher defect density enhances non-radiative relaxation, resulting in lower PL intensity.[36–38] The introduction of selenium into the kesterite lattice not only increased the PL intensity but also caused a red shift in the PL peak from 930 nm (1.33 eV) in ACZTS to 1132 nm (1.1 eV) in ACZTSSe, suggesting a reduction in bandgap energy upon selenization. The improved PL intensity in ACZTSSe films is indicative of reduced defect density, particularly a reduction in Sn–Zn-poor defects, which is linked to the incorporation of the larger selenium atom.[15,25] Furthermore, this could also be explained by a lower Cu/(Zn + Sn) ratio in the ACZTSSe films, as selenization prevents Zn and Sn losses observed in the ACZTS films. The reduced Cu/(Zn + Sn) ratio effectively narrows the bandgap of the ACZTSSe films.

To further investigate carrier dynamics, TRPL measurements were performed, with results depicted in Fig. 5(b). The TRPL decay curves were fitted using an exponential model as Eq. (1),

$$I(t) = I_0 e^{(-t/\tau)}, \tag{1}$$

where I_0 represents the initial PL intensity, t is the delay time, and τ is the carrier lifetime.[39] The average carrier lifetime of the ACZTS films was measured at 1.05 ns, significantly shorter than the 2.49 ns observed for the ACZTSSe films. This extension in carrier lifetime after selenization corresponds to a reduction in non-radiative recombination centers, further corroborating the lower defect density in the ACZTSSe films. It emphasizes the improved carrier dynamics in the ACZTSSe films, reflecting the reduced prevalence of non-radiative recombination centers. These findings collectively demonstrate that ACZTSSe films exhibit superior optical properties, attributable to enhanced structural quality and reduced defect density compared to ACZTS films. The measured TRPL lifetimes are comparable to prior reports for similar films. Although some record-efficiency kesterites show lifetimes >5 ns, those cases typically involve additional defect passivation. Importantly, recent

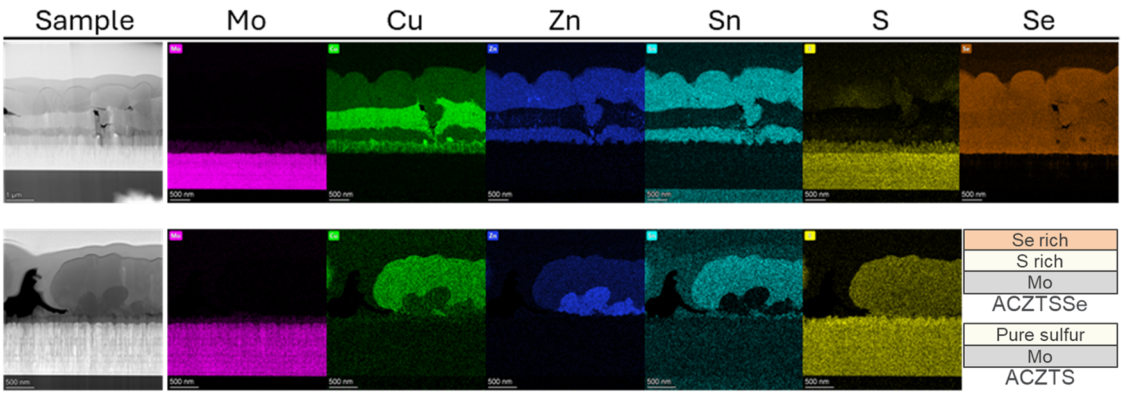

FIG. 4. HAADF STEM and STEM-EDS mapping images for different elements of ACZTSSe (top) and ACZTS (bottom) thin-films. The accompanying schematic illustrates a comparison of the layer structures of these two samples.

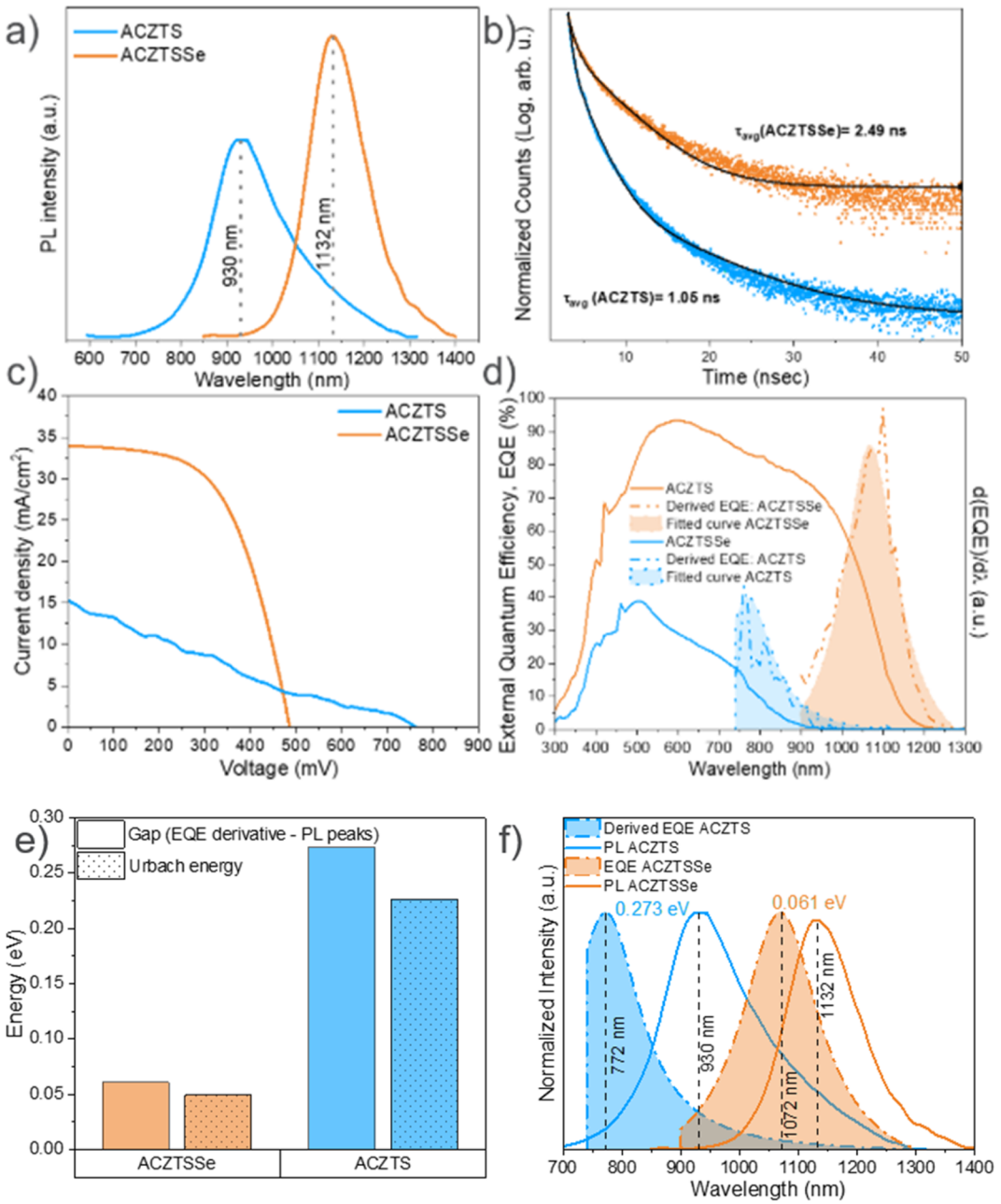

FIG. 5. (a) PL and (b) TRPL spectra of ACZTS and ACZTSSe thin-films. (c) J–V curves with, (d) EQE spectra with first derivatives to determine bandgaps, (e) UE, and (f) bandgap differences ($E_g^{EQE} - E_g^{PL}$) for ACZTS and ACZTSSe devices.

studies note that TRPL lifetimes in CZTSSe do not directly correlate with device performance because trapping dominates the decay.[40] Thus, our double-exponential fits represent trap-limited effective lifetimes, confirming significant defect-mediated recombination in the bulk and interfaces. Recent literature emphasizes that kesterite cells suffer from persistent deficits due to Cu–Zn antisite disorder, Sn-related defect complexes, and band-tail states.[41] High-efficiency kesterite devices have largely suppressed band-tail losses, but deep defects and grain-boundary/interface recombination remain the dominant loss mechanisms.

Solar cell devices were fabricated using a substrate configuration of Mo/absorber/CdS/i-ZnO/ITO, where the absorber layer consists of either ACZTS or ACZTSSe thin films. Device performance was evaluated using J–V measurements. The J–V characteristics of

the ACZTS and ACZTSSe devices are shown in Fig. 5(c), measured over an active area of 0.16 cm^2. The ACZTSSe-based device achieved a PCE of 9.35%, with an V_{OC} of 486 mV, a short-circuit current density (J_{SC}) of 34.0 mA/cm^2, and a fill factor (FF) of 56.7%. In contrast, the ACZTS-based device demonstrated significantly lower performance, with a PCE of 2.35%, V_{OC} of 770 mV, J_{SC} of 15.3 mA/cm^2, and FF of 23.3%. Notably, the V_{OC} of 770 mV is among the highest reported for kesterite-based solar cells and notably higher than that of the ACZTSSe device.[42,43] Despite the relatively high V_{OC} of the ACZTS device, its low J_{SC} and FF may indicate that carrier extraction is severely limited. This combination suggests that, although a functional p–n junction is formed, the device performance may be dominated by transport-related losses rather than purely bulk recombination. It is reported in the literature that non-ideal band alignment (cliff) at the CdS/ACZTS interface introduces a barrier for electron extraction, leading to suppressed current collection and reduced FF.[5,44,45] Such behavior is often associated with transport barriers or interface recombination, where a sufficiently high built-in potential supports a high V_{OC}, while inefficient carrier extraction limits J_{SC} and FF. Therefore, the device performance suggests that interface energetics and transport limitations, rather than only intrinsic defect density, play a dominant role in limiting the efficiency of the ACZTS device. Wide bandgap kesterite requires alternative buffer layers, such as Zn(O, S), ZnSnO,[46] or gradient interface approaches.[13] In addition, the ACZTS cell shows series resistance and shunt resistance, confirming its low FF. No additional metallic grid was used; thus, the series resistance is partially influenced by the sheet resistance of the ITO layer. No distinct S-shaped kink is present, but the increased series resistance values imply a significant contact barrier. In kesterite cells, thick MoS_2 at the Mo interface is known to increase the series resistance and suppress FF.[47] Conversely, a thin Ag layer in ACZTS has been reported to suppress MoS_2 and reduce transport resistance.[47,48] Interface passivation layers (e.g., Al_2O_3) often increase V_{OC} while reducing FF due to increased series resistance.[49] These observations suggest that the very low FF in our ACZTS device arises from residual transport limitations (back-contact/interfacial resistance) in addition to defect-related recombination.

Figure 5(d) presents the EQE spectra, from which the optical bandgaps were estimated. The ACZTS film exhibits 1.61 eV, which is higher than the 1.16 eV bandgap of the ACZTSSe film. The EQE and PL measurements of our kesterite-based solar cell show a discrepancy, with the EQE onset at 750 nm (1.65 eV) and the PL peak at 930 nm (1.33 eV). This difference is primarily attributed to significant band tailing in the absorber, arising from localized states extending into the nominal bandgap, as well as cation disorder between Zn and Cu atoms. While EQE reflects carrier generation and transport across extended states, PL is dominated by radiative recombination from band-tail states.[50] As a result, PL underestimates the optical bandgap, whereas EQE provides a more accurate representation of the transport gap relevant for device operation. The higher bandgap of the ACZTS thin film contributes to the enhanced V_{OC}. Despite the higher V_{OC}, the overall performance of the ACZTS device was inferior to that of the ACZTSSe device. One of the reasons for performance disparity may be explained by the lower formation energy of Cu–Zn antisite defects in the ACZTS films, as reported in previous studies, which leads to the creation of numerous defects.[36–38] These defects likely reduced low carrier lifetime and contributed to the observed inferior J–V performance. Moreover, the presence of a high concentration of defects in the ACZTS films likely resulted in the formation of deep energy levels within the bandgap. These defect-related states can be probed by calculating the Urbach energy (UE) at the tail states of the EQE spectrum.[51] The calculated UE for the ACZTS device was 226 meV, significantly higher than the 49 meV measured for the ACZTSSe devices, as shown in the bar graph in Fig. 5(e). This large discrepancy in UE values further support the notion of defect-related states impeding the performance of the ACZTS devices. The calculated difference between the bandgap of the films and their radiative bandgap ($E_g^{EQE} - E_g^{PL}$) further corroborates this observation.[52,53] For the

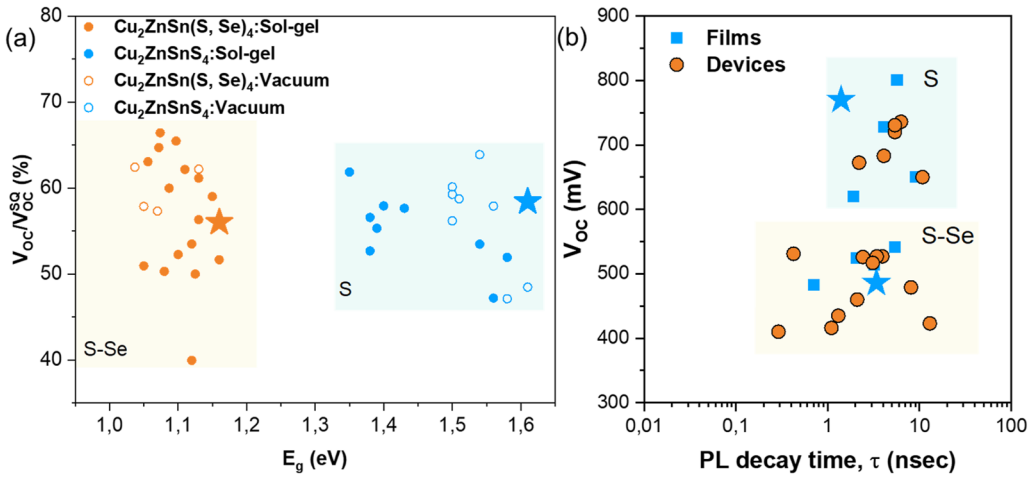

FIG. 6. (a) V_{OC}/V_{OC}^{SQ} values vs E_g and (b) carrier lifetimes vs V_{OC} for reported high-performance kesterite solar cells, with values for ACZTS and ACZTSSe devices from this work marked by blue and orange asterisks, respectively.

ACZTS device, the difference was 273 meV, while for the ACZTSSe devices, it was only 61 meV, as shown in Fig. 5(f). These results consistently indicate that increased band tailing and defect-related states play a critical role in limiting the performance of the ACZTS device.

This observation is in strong agreement with recent literature,[3] which identifies key bottlenecks in kesterite photovoltaics, including the V_{OC} deficit, band tailing, cation disorder, defect complex formation, and the influence of compositional grading. Addressing these limitations through interface engineering, crystallization control, and defect management represents a critical pathway toward improving wide-bandgap kesterite device performance.

To evaluate the quality of the fabricated films relative to the global state-of-the-art, the V_{OC} deficit was assessed by calculating the ratio of the measured V_{OC} to the theoretical limit V_{OC}^{SQ} predicted by the Shockley–Queisser (SQ) model.[54] This metric provides a robust comparison of solar cells with different bandgaps. The V_{OC}/V_{OC}^{SQ} values achieved by high-performance kesterite solar cells and their corresponding Eg^{EQE} are presented in Fig. 6(a). Notably, reported wide- and narrow-bandgap devices have achieved V_{OC}/V_{OC}^{SQ} values exceeding 50%, with global champion values reaching 63.8% for pure S devices[12] and 64.2% for S–Se devices.[27] In this study, the V_{OC}/V_{OC}^{SQ} values for the ACZTS and ACZTSSe devices were 58.4% and 56.0%, respectively, closely approaching the reported global champion values. Since V_{OC} is directly linked to carrier dynamics, the quality of the films was further validated by comparing the carrier lifetimes obtained in this work with the lifetimes corresponding to reported high-performance devices, which is shown in Fig. 6(b). It illustrates the correlation between reported carrier lifetimes and V_{OC} for both bare films and complete devices. The typical carrier lifetime range for high-performing wide- and narrow-bandgap materials lies between 1 and 10 ns. In addition, the carrier lifetimes associated with the reported champion devices' V_{OC} were ~5.44 ns for narrow-bandgap thin-films and 5.8 ns for wide-bandgap thin-films.[12,55] The carrier lifetimes for the ACZTS and ACZTSSe films in this work are 1.05 and 2.49 ns, respectively. These values fall within the reported range for high-performing films, further demonstrating the competitive quality of the fabricated devices.

CONCLUSION

This study highlights the impact of Se incorporation on the optoelectronic properties and device performance of ACZTS and ACZTSSe thin-films for kesterite-based solar cells. XRD and Raman analyses confirmed successful Se incorporation, resulting in lattice expansion and red-shifted Raman and PL peaks, in accordance with a change in composition that also leads to a reducing bandgap from 1.61 eV (ACZTS) to 1.16 eV (ACZTSSe). Surprisingly, SEM and STEM images show films that are rather non-uniform distribution of phases that are typically not identified in XRD and Raman. PL and TRPL measurements revealed higher PL intensity and longer carrier lifetimes for ACZTSSe films, reflecting improved crystallinity and reduced non-radiative recombination. J–V measurements demonstrated a significant increase in efficiency from 2.35% (ACZTS) to 9.35% (ACZTSSe), attributed to lower defect density, reduced EU, and enhanced carrier dynamics, as evidenced by higher lifetimes and smaller energy gap differences between radiative and non-radiative recombination. Although ACZTS exhibited a higher V_{OC}, the superior performance of ACZTSSe devices highlights the role of Se in defect passivation and carrier transport. The calculated V_{OC}/V_{OC}^{SQ} values for ACZTS and ACZTSSe devices closely approach globally reported champion values, reaffirming the competitiveness of these materials. This work provides critical insights into optimizing kesterite thin-films, emphasizing the importance of compositional control, defect mitigation, and carrier dynamics to achieve high-efficiency solar cells.

ACKNOWLEDGMENTS

M.G., G.V., S.S., B.V., B.S., J.T., P.S., and S. Shukla acknowledge KESPER from (M-ERA.NET) Grant Agreement No. 958174, for supporting this research. J.T. acknowledged Fundação para a CiÊncia e técnologia (FCT) under Project No. 2021.02405.CEECIND. M.G. and S.S. acknowledge the funding received from the European Union's Horizon 2020 research and innovation program under the Marie Skłodowska-Curie Grant Agreement Nos. 101208825 and 101208369, respectively. D.S acknowledges funds from the Fonds voor Wetenschappelijk Onderzoek—Vlaanderen (FWO) for the fellowship (Grant No. 11PJZ24N). I.D.T. acknowledges funds from the Fonds voor Wetenschappelijk Onderzoek—Vlaanderen (FWO) for the Fellowship No. 11PNM24N.

AUTHOR DECLARATIONS

Conflict of Interest

The authors have no conflicts to disclose.

Author Contributions

Mina Ghorbani, Sunil Suresh, and Gautam Virenutan contributed equally to this work.

Mina Ghorbani: Data curation (equal); Formal analysis (equal); Investigation (equal); Writing – original draft (equal); Writing – review & editing (equal). **Sunil Suresh**: Formal analysis (equal); Investigation (equal); Writing – original draft (equal); Writing – review & editing (equal). **Gautam Virenutan**: Data curation (lead); Formal analysis (equal); Investigation (equal); Writing – original draft (lead); Writing – review & editing (equal). **Guy Brammertz**: Formal analysis (supporting); Investigation (supporting); Writing – review & editing (supporting). **Vishal Kakkarakunnel Jose**: Investigation (supporting). **Daniely Santos**: Formal analysis (supporting); Investigation (supporting); Writing – original draft (supporting); Writing – review & editing (supporting). **Irene Dei Tos**: Investigation (supporting). **Bárbara Sieira**: Formal analysis (supporting); Investigation (supporting); Writing – review & editing (supporting). **Jennifer Teixeira**: Formal analysis (supporting); Investigation (supporting); Writing – original draft (supporting); Writing – review & editing (supporting). **Pedro Salomé**: Formal analysis (supporting); Funding acquisition (equal); Supervision (supporting); Writing – original draft (supporting); Writing – review & editing (supporting). **Sudhanshu Shukla**: Conceptualization (equal); Data curation (equal); Formal analysis (equal); Funding acquisition (equal); Supervision (equal); Writing – original draft (equal); Writing – review & editing (equal). **Bart Vermang**: Conceptualization (equal);

Data curation (equal); Funding acquisition (equal); Supervision (equal); Writing – original draft (equal); Writing – review & editing (equal).

DATA AVAILABILITY

The data that support the findings of this study are available within the article.

REFERENCES

[1] S. Suresh, D. J. Rokke, A. A. Drew, E. Alruqobah, R. Agrawal, and A. R. Uhl, "Extrinsic doping of ink-based Cu(In,Ga)(S,Se)$_2$-absorbers for photovoltaic applications," Adv. Energy Mater. **12**, 2103961 (2022).

[2] A. O. Ali, A. T. Elgohr, M. H. El-Mahdy, H. M. Zohir, A. Z. Emam, M. G. Mostafa, M. Al-Razgan, H. M. Kasem, and M. S. Elhadidy, "Advancements in photovoltaic technology: A comprehensive review of recent advances and future prospects," Energy Convers. Manage.: X **26**, 100952 (2025).

[3] I. Poli *et al.*, "Lead-free perovskites and derivatives for photogeneration: A roadmap to sustainable approaches for photovoltaics and photo(electro)catalysis," J. Phys.: Energy **8**, 011501 (2026).

[4] J. Li, K. Sun, X. Yuan, J. Huang, M. A. Green, and X. Hao, "Emergence of flexible kesterite solar cells: Progress and perspectives," npj Flexible Electron. **7**, 16 (2023).

[5] Nisika, K. Kaur, and M. Kumar, "Progress and prospects of CZTSSe/CdS interface engineering to combat high open-circuit voltage deficit of kesterite photovoltaics: A critical review," J. Mater. Chem. A **8**, 21547 (2020).

[6] K. Kaur, N. Kumar, and M. Kumar, "Strategic review of interface carrier recombination in Earth abundant Cu–Zn–Sn–S–Se solar cells: Current challenges and future prospects," J. Mater. Chem. A **5**, 3069 (2017).

[7] G. Tseberlidis, C. Gobbo, V. Trifiletti, V. Di Palma, and S. Binetti, "Cd-free kesterite solar cells: State-of-the-art and perspectives," Sustainable Mater. Technol. **41**, e01003 (2024).

[8] J. Fu *et al.*, "A critical review of solution-process engineering for kesterite thin-film solar cells: Current strategies and prospects," J. Mater. Chem. A **12**, 545 (2024).

[9] A. Jimenez-Arguijo *et al.*, "Formation pathway of high-efficiency kesterite solar cells fabricated through molecular ink chemistry," Nat. Energy **11**, 194 (2026).

[10] C. Cui *et al.*, "Regulating grain growth via Li_2SnS_3 interphase in kesterite solar cells with certified efficiencies exceeding 15%," Nat. Energy **11**, 460 (2026).

[11] M. Jiao *et al.*, "Suppressing defects in kesterite solar cells via balanced phase evolution to enable 15.1% certified record efficiency," Joule **2026**, 102345.

[12] A. Wang *et al.*, "Cd-free pure sulfide kesterite Cu_2ZnSnS_4 solar cell with over 800 mV open-circuit voltage enabled by phase evolution intervention," Adv. Mater. **36**, 2307733 (2023).

[13] K. Yin *et al.*, "Gradient bandgaps in sulfide kesterite solar cells enable over 13% certified efficiency," Nat. Energy **10**, 205 (2025).

[14] A. Polizzotti, I. L. Repins, R. Noufi, S.-H. Wei, and D. B. Mitzi, "The state and future prospects of kesterite photovoltaics," Energy Environ. Sci. **6**, 3171 (2013).

[15] Y. E. Romanyuk *et al.*, "Doping and alloying of kesterites," J. Phys.: Energy **1**, 044004 (2019).

[16] S. Suresh and A. R. Uhl, "Present status of solution-processing routes for Cu(In,Ga)(S,Se)$_2$ solar cell absorbers," Adv. Energy Mater. **11**, 2003743 (2021).

[17] J. Zhou *et al.*, "Control of the phase evolution of kesterite by tuning of the selenium partial pressure for solar cells with 13.8% certified efficiency," Nat. Energy **8**, 526 (2023).

[18] J. Park, J.-G. Song, T. Choi, S. Sim, H. Choi, S. W. Han, H.-B.-R. Lee, S.-H. Kim, and H. Kim, "Comparison of hydrogen sulfide gas and sulfur powder for synthesis of molybdenum disulfide nanosheets," Curr. Appl. Phys. **16**, 691 (2016).

[19] I. Akyuz, F. Atay, R. Aydin, and S. Kose, "Production and characterization of CZTS films: On the role of H_2S flow rate," Sol. Energy **194**, 709 (2019).

[20] J. H. Lee, H. J. Choi, W. M. Kim, J. H. Jeong, and J. K. Park, "Effect of pre-annealing on the phase formation and efficiency of CZTS solar cell prepared by sulfurization of Zn/(Cu,Sn) precursor with H_2S gas," Sol. Energy **136**, 499 (2016).

[21] R. Scaffidi, G. Brammertz, Y. Wang, A. U. Zaman, K. Sasikumar, J. de Wild, D. Flandre, and B. Vermang, "A study of bandgap-graded CZTGSe kesterite thin films for solar cell applications," Energy Adv. **2**, 1626 (2023).

[22] J. Li, H. Wang, L. Wu, C. Chen, Z. Zhou, F. Liu, Y. Sun, J. Han, and Y. Zhang, "Growth of $Cu_2ZnSnSe_4$ film under controllable Se vapor composition and impact of low Cu content on solar cell efficiency," ACS Appl. Mater. Interfaces **8**, 10283 (2016).

[23] S. G. Haass, M. Diethelm, M. Werner, B. Bissig, Y. E. Romanyuk, and A. N. Tiwari, "11.2% efficient solution processed kesterite solar cell with a low voltage deficit," Adv. Energy Mater. **5**, 1500712 (2015).

[24] J. J. Scragg, T. Kubart, J. T. Wätjen, T. Ericson, M. K. Linnarsson, and C. Platzer-Björkman, "Effects of back contact instability on Cu_2ZnSnS_4 devices and processes," Chem. Mater. **25**, 3162 (2013).

[25] A. Walsh, S. Chen, S. Wei, and X. Gong, "Kesterite thin-film solar cells: Advances in materials modelling of Cu_2ZnSnS_4," Adv. Energy Mater. **2**, 400 (2012).

[26] M. Dimitrievska, H. Xie, A. Fairbrother, X. Fontané, G. Gurieva, E. Saucedo, A. Pérez-Rodríguez, S. Schorr, and V. Izquierdo-Roca, "Multiwavelength excitation Raman scattering of $Cu_2ZnSn(S_xSe_{1-x})_4$ ($0 \le x \le 1$) polycrystalline thin films: Vibrational properties of sulfoselenide solid solutions," Appl. Phys. Lett. **105**, 031913 (2014).

[27] Y. Gong *et al.*, "Ag incorporation with controlled grain growth enables 12.5% efficient kesterite solar cell with open circuit voltage reached 64.2% Shockley–Queisser limit," Adv. Funct. Mater. **31**, 2101927 (2021).

[28] M. Pal, N. R. Mathews, F. Paraguay-Delgado, and X. Mathew, "Phase controlled solvothermal synthesis of Cu_2ZnSnS_4, $Cu_2ZnSn(S,Se)_4$ and $Cu_2ZnSnSe_4$ nanocrystals: The effect of Se and S sources on phase purity," Mater. Chem. Phys. **166**, 201 (2015).

[29] X. Xu *et al.*, "Controlling selenization equilibrium enables high-quality kesterite absorbers for efficient solar cells," Nat. Commun. **14**, 6650 (2023).

[30] J. Li *et al.*, "Unveiling microscopic carrier loss mechanisms in 12% efficient $Cu_2ZnSnSe_4$ solar cells," Nat. Energy **7**, 754 (2022).

[31] Y. Li, C. Cui, H. Wei, Z. Shao, Z. Wu, S. Zhang, X. Wang, S. Pang, and G. Cui, "Suppressing element inhomogeneity enables 14.9% efficiency CZTSSe solar cells," Adv. Mater. **36**, 2400138 (2024).

[32] C. Xiang *et al.*, "Solution-processed kesterite solar module with 10.1% certified efficiency," Nat. Energy **10**, 1315 (2025).

[33] J. M. Skelton, A. J. Jackson, M. Dimitrievska, S. K. Wallace, and A. Walsh, "Vibrational spectra and lattice thermal conductivity of kesterite-structured Cu_2ZnSnS_4 and $Cu_2ZnSnSe_4$," APL Mater. **3**, 041102 (2015).

[34] M. Dimitrievska, A. Fairbrother, X. Fontané, T. Jawhari, V. Izquierdo-Roca, E. Saucedo, and A. Pérez-Rodríguez, "Multiwavelength excitation Raman scattering study of polycrystalline kesterite Cu_2ZnSnS_4 thin films," Appl. Phys. Lett. **104**, 021901 (2014).

[35] V. Campanari *et al.*, "Reevaluation of photoluminescence intensity as an indicator of efficiency in perovskite solar cells," Sol. RRL **6**, 2200049 (2022).

[36] H. Duan, W. Yang, B. Bob, C. Hsu, B. Lei, and Y. Yang, "The role of sulfur in solution-processed $Cu_2ZnSn(S,Se)_4$ and its effect on defect properties," Adv. Funct. Mater. **23**, 1466 (2012).

[37] S. Wu, C. Chang, H. Chen, C. Shih, Y. Wang, C. Li, and S. Chan, "High-efficiency $Cu_2ZnSn(S,Se)_4$ solar cells fabricated through a low-cost solution process and a two-step heat treatment," Prog. Photovoltaics **25**, 58 (2016).

[38] J. Li, S. Kim, D. Nam, X. Liu, J. Kim, H. Cheong, W. Liu, H. Li, Y. Sun, and Y. Zhang, "Tailoring the defects and carrier density for beyond 10% efficient CZTSe thin film solar cells," Sol. Energy Mater. Sol. Cells **159**, 447 (2017).

[39] C. J. Hages, A. Redinger, S. Levcenko, H. Hempel, M. J. Koeper, R. Agrawal, D. Greiner, C. A. Kaufmann, and T. Unold, "Identifying the real minority carrier lifetime in nonideal semiconductors: A case study of kesterite materials," Adv. Energy Mater. **7**, 1700167 (2017).

[40] S. S. Hadke, Z. Su, Q. Meng, H. Xin, S. Wu, G. Liang, Z. Shao, and L. H. Wong, "Understanding efficiency losses from radiative and nonradiative recombination in $Cu_2ZnSn(S,Se)_4$ solar cells," Nat. Commun. **16**, 8240 (2025).

[41] Y. S. Ocak and F. Bayansal, "Advancing Earth-abundant CZTSSe solar cells: Recent progress in efficiency and defect engineering," Nanomaterials **15**, 1617 (2025).

[42]J. K. Larsen *et al.*, "Cadmium free Cu_2ZnSnS_4 solar cells with 9.7% efficiency," Adv. Energy Mater. **9**, 1900439 (2019).
[43]X. Cui *et al.*, "Cd-Free Cu_2ZnSnS_4 solar cell with an efficiency greater than 10% enabled by Al_2O_3 passivation layers," Energy Environ. Sci. **12**, 2751 (2019).
[44]H. Bencherif, "Towards a high efficient Cd-free double CZTS layers kesterite solar cell using an optimized interface band alignment," Sol. Energy **238**, 114 (2022).
[45]X. Liu, J. Guo, R. Hao, Q. Zhao, F. Chang, L. Wang, B. Liu, Y. Li, and K. Gu, "Cliff-like conduction band offset at CdS/Cu_2ZnSnS_4 heterojunction prepared by sputtering CuSn alloy target using different stacking order," Sol. Energy **183**, 285 (2019).
[46]A. Wang *et al.*, "Hydrogen-enhanced carrier collection enabling wide-bandgap Cd-free Cu_2ZnSnS_4 solar cells with 11.4% certified efficiency," Nat. Energy **10**, 255 (2025).
[47]H. Honarvar Nazari and T. P. Dhakal, "Influence of Ag-doping on the performance of Cu_2ZnSnS_4 solar cells," Sol. Energy **253**, 321 (2023).
[48]L. P. Mwakyusa, L. Leist, M. Rinke, A. Welle, U. W. Paetzold, B. S. Richards, and M. Hetterich, "Impact of silver incorporation at the back contact of Kesterite solar cells on structural and device properties," Thin Solid Films **709**, 138223 (2020).
[49]E. Ojeda-Durán, K. Monfil-Leyva, J. Andrade-Arvizu, I. Becerril-Romero, Y. Sánchez, R. Fonoll-Rubio, M. Guc, Z. J. Li-Kao, J. A. Luna-López, and E. Saucedo, "High efficiency Cu_2ZnSnS_4 solar cells over FTO substrates and their CZTS/CdS interface passivation via thermal evaporation of Al_2O_3," J. Mater. Chem. C **9**, 5356 (2021).
[50]S. Siebentritt, G. Rey, A. Finger, D. Regesch, J. Sendler, T. P. Weiss, and T. Bertram, "What is the bandgap of kesterite?," Sol. Energy Mater. Sol. Cells **158**, 126 (2016).
[51]Y. Gong *et al.*, "Elemental de-mixing-induced epitaxial kesterite/CdS interface enabling 13%-efficiency kesterite solar cells," Nat. Energy **7**, 966 (2022).
[52]M. Grossberg, J. Krustok, J. Raudoja, and T. Raadik, "The role of structural properties on deep defect states in Cu_2ZnSnS_4 studied by photoluminescence spectroscopy," Appl. Phys. Lett. **101**, 102102 (2012).
[53]K. Tanaka, T. Shinji, and H. Uchiki, "Photoluminescence from Cu_2ZnSnS_4 thin films with different compositions fabricated by a sputtering-sulfurization method," Sol. Energy Mater. Sol. Cells **126**, 143 (2014).
[54]W. Shockley and H. J. Queisser, "Detailed balance limit of efficiency of *p-n* junction solar cells," J. Appl. Phys. **32**, 510 (1961).
[55]H. Wei *et al.*, "Regulating hetero-nucleation enabling over 14% efficient kesterite solar cells," Small **20**, 2308266 (2023).